Research Article Vol. 30, No. 5 / 28 Feb 2022 / Optics Express 6640
Optics EXPRESS

An evaluation of remote sensing algorithms for the estimation of diffuse attenuation coefficients in the ultraviolet bands

YONGCHAO WANG,[1] ZHONGPING LEE,[2,*] MICHAEL ONDRUSEK,[3] XU LI,[1] SHUAI ZHANG,[2] AND JINGYU WU[4]

[1]State Key Laboratory of Marine Environmental Science, Xiamen University, Xiamen, 361102, China
[2]School for the Environment, University of Massachusetts Boston, Boston, MA 02125, USA
[3]NOAA Center for Satellite Applications and Research, College Park, MD 20740, USA
[4]Research and Development Center for Ocean Observation Technologies, Xiamen University, Xiamen, 361102, China
*ZhongPing.Lee@umb.edu

Abstract: In this study, six algorithms (both empirical and semi-analytical) developed for the estimation of K_d in the ultraviolet (UV) domain (specifically 360, 380, and 400 nm) were evaluated from a dataset of 316 stations covering oligotrophic ocean and coastal waters. In particular, the semi-analytical algorithm (Lee et al. 2013) used remote sensing reflectance in these near-blue UV bands estimated from a recently developed deep learning system as the input. For $K_d(380)$ in a range of 0.018 - 2.34 m^{-1}, it is found that the semi-analytical algorithm has the best performance, where the mean absolute relative difference (MARD) is 0.19, and the coefficient of determination (R^2) is 0.94. For the empirical algorithms, the MARD values are 0.23–0.90, with R^2 as 0.70–0.92, for this evaluation dataset. For a VIIRS and *in situ* matchup dataset (N = 62), the MARD of $K_d(380)$ is 0.21 (R^2 as 0.94) by the semi-analytical algorithm. These results indicate that a combination of deep learning system and semi-analytical algorithms can provide reliable K_d(UV) for past and present satellite ocean color missions that have no spectral bands in the UV, where global K_d(UV) products are required for comprehensive studies of UV radiation on marine primary productivity and biogeochemical processes in the ocean.

1. Introduction

Ultraviolet (UV) radiation has a complex impact on aquatic ecosystems [1]. It could be an energy source for phytoplankton [2], may also prohibit phytoplankton growth, can contribute to the photochemical transformation of dissolved organic matter (DOM) [3,4], and can affect the vertical movement of zooplankton [5]. In addition, ultraviolet radiation modulates the release of methane and other climate-related gases by phytoplankton cells, which directly contributes to global climate change [6]. Thus, quantifying UV radiation in ocean is an important task for a wide range of oceanographic studies. The amount of UV radiation reaching the ocean surface is primarily determined by the layer of ozone in the atmosphere, which is further modulated by water's attenuation when UV radiation propagates from surface to deeper depths [1,7]. This attenuation parameter is commonly termed as the diffuse attenuation coefficient of downwelling irradiance (K_d; m^{-1}). While UV radiation at surface varies in space and time, K_d, an important apparent optical property [8], also varies with water constituents. Therefore, to evaluate and understand UV related processes in the ocean, it is necessary to accurately map the spatial variation of K_d in the UV domain year around [9,10], a task that could only be achieved from satellite measurements.

The traditional satellites aimed at ocean's bio-optical properties, such as the Coastal Zone Color Scanner (CZCS), Sea-viewing Wide Field-of-view (SeaWiFS), Moderate Resolution

#446114 https://doi.org/10.1364/OE.446114
Journal © 2022 Received 18 Oct 2021; revised 18 Dec 2021; accepted 23 Dec 2021; published 15 Feb 2022

Optics EXPRESS

Imaging Spectroradiometer (MODIS), Medium Resolution Imaging Spectrometer (MERIS), Visible Infrared Imaging Radiometer Suite (VIIRS), etc., however, don't have spectral bands shorter than 410 nm, thus it is a challenge to obtain global K_d properties in the UV from these ocean color satellites. While modern ocean color satellites start to include bands in the UV (e.g., Plankton, Aerosol, Cloud and ocean Ecosystem (PACE), Second generation Global Imager (SGLI), Ocean and Land Colour Instrument (OLCI), etc.), sophisticated algorithms must be developed in order to generate products in the UV for the earlier satellites, so that UV properties in the ocean could be extended back 20 + years. For this goal, as described in more details in Section 2, various algorithms have been developed in the past decades for the estimation of K_d in the UV (termed as K_d(UV) in the following, with the shortest wavelength limited to 360 nm here), either for one specific wavelength or many wavelengths [10–12]. But the applicability of these algorithms for global applications has not been evaluated. More importantly, most of these algorithms are empirical [9,13–15], where their applicability is usually limited to the data or region used during the phase of algorithm development. Recently it is found that remote sensing reflectance (R_{rs}, sr^{-1}) in the near-blue UV bands (360–400 nm) can be well estimated from R_{rs} in the visible bands using deep-learning approaches [16,17], thus it is possible to employ a semi-analytical algorithm to estimate K_d(UV) for data obtained by traditional ocean color satellites.

Thus in this study, based on measurements from oligotrophic ocean to coastal waters, we evaluated six algorithms developed for K_d(UV), as well as a performance with VIIRS measurements. This paper is such organized that Section 2 describes the six algorithms (empirical and semi-analytical); Section 3 provides information of both field measured data and satellite data used for algorithm evaluations; Section 4 presents results and discussion about these algorithms; and Section 5 summarizes our findings and presents some future prospects.

2. Brief description of algorithms for K_d(UV)

A wide range of algorithms have been developed for the estimation of K_d(UV) in the past decades [9–12,14,15,18,19]. These can be grouped into empirical and semi-analytical algorithms, with empirical algorithms including one-step and multi-step schemes. A brief description of the essence of such representative algorithms is provided below.

2.1. One-step empirical algorithm (J2003)

Based on field-measured data (53 stations, K_d(380) in a range of 0.034 - 4.4 m^{-1}) in the Mid-Atlantic Gulf and the Bering Sea from 1996 to 1998, following the scheme for K_d(490) [20,21], Johannessen et al. [11] developed a simple empirical relationship between the ratio of R_{rs} and K_d(380),

$$K_d(380) = 0.302\left(\frac{R_{rs}(412)}{R_{rs}(555)}\right)^{-1.24}. \quad (1)$$

Here $R_{rs}(sr^{-1})$ is the remote sensing reflectance of a water body, which is defined as the ratio of water-leaving radiance to downwelling irradiance just above the surface. R_{rs} is a standard product for many satellite ocean color missions.

2.2. Two-step empirical algorithm (M2001)

Centered on the "Case 1" concept and system, Morel and Maritorena [12] developed empirical relationships between K_d and chlorophyll concentration ([Chl], mg/m^3) based on nearly 30 years

Optics EXPRESS

of measurements (1969–1996, total 255 data stations). The relationship is written as:

$$K_d(\lambda) = K_w(\lambda) + \mathcal{X}(\lambda) \times [Chl]^{e(\lambda)}, \tag{2a}$$

$$K_w(\lambda) = a_w(\lambda) + b_{bw}(\lambda). \tag{2b}$$

Here χ and e are empirical coefficients developed from the dataset, while a_w and b_{bw} are the absorption and backscattering coefficients of pure seawater. In the development of this scheme [12], values of $a_w(\lambda)$ were taken from the literature [22,23], with values of $b_{\mathrm{bw}}(\lambda)$ from Morel [24]. Although both a_w and b_{bw} values were revised in the recent decade [25,26], but we used the a_w and b_{bw} values originally adopted for this scheme, as χ and e were estimated using those a_w and b_{bw} values. For the estimation of K_d, [Chl] is a standard product from ocean color satellites, which is generally produced using empirical algorithms [27],

$$[\mathrm{Chl}] = 10^{\alpha_0+\alpha_1\times \mathrm{RR}+\alpha_2\times \mathrm{RR}^2+\alpha_3\times \mathrm{RR}^3+\alpha_4\times \mathrm{RR}^4}, \tag{3a}$$

$$\mathrm{RR} = \log_{10}\left(\frac{\mathrm{Max}(R_{rs}(\lambda_1), R_{rs}(\lambda_2), R_{rs}(\lambda_3))}{R_{rs}(\lambda_4)}\right). \tag{3b}$$

Here $\lambda_{1\sim3}$ are wavelengths in the range between 440 and 510 nm, and λ_4 is around 550 nm. $\alpha_{0\sim4}$ are empirical coefficients derived by pooling global measurements.

2.3. Empirical algorithm based on principal component analysis (C2014)

Fichot et al. [9] and Cao et al. [14] used principal component analysis (PCA) to decompose an R_{rs} dataset into a few principal components (PCs). For a given R_{rs} spectrum, the scores of the first four PCs are used as predictors of $K_d(\lambda)$ (the algorithm is termed as SeaUV and SeaUVc), written as

$$Ln(K_d(\lambda)) = \alpha + \beta \times PC_1 + \gamma \times PC_2 + \delta \times PC_3 + \varepsilon \times PC_4, \tag{4}$$

where α, β, γ, δ, and ε are empirical coefficients [9,14], while PC_{1-4} are the scores from the principal component analysis. Since SeaUVc [14] is an updated version and performed better in the data studied [9,14], this effort focused on SeaUVc, with its processing based on the value of $K_{\mathrm{d}}(490)$ (another standard product from satellite ocean color missions). When $K_{\mathrm{d}}(490) > 0.32\ \mathrm{m}^{-1}$, the updated SeaUVc of Cao et al. [14] is used, otherwise, SeaUVc of Fichot et al. [9] is used, so by design this scheme is intended for application of both clear and turbid waters.

2.4. Multi-step empirical algorithm (V2001)

Two decades ago, Vasilkov et al. [10] developed a K_d(UV) algorithm based on a relationship between K_d and the inherent optical properties (IOPs) [8]. From data obtained via Monte Carlo simulations, Gordon [28] modeled subsurface K_d as a function of water's absorption (a) and backscattering (b_{b}) coefficients as:

$$K_d(\lambda)/D_0 = 1.0395(a(\lambda) + b_b(\lambda)), \tag{5a}$$

$$D_0 = f/\cos(\theta_{0w}) + 1.197(1-f), \tag{5b}$$

where f is the fraction of direct sunlight in the incident irradiance transmitted through the sea surface under clear sky, θ_{0w} is the solar zenith angle in water. The value of f can be calculated based on solar zenith angle and wavelength from atmospheric models. It then requires values of a and b_{b} for the calculation of K_{d}. Vasilkov et al. [10] used [Chl] and empirical averages

Optics EXPRESS

of phytoplankton-specific absorption coefficients for the estimations. Specifically, a and b_b are modeled as [29–31]:

$$a(\lambda) = a_w(\lambda) + a_{ph}(\lambda) + a_{DOM}(\lambda). \tag{6a}$$

$$b_b(\lambda) = b_{bw}(\lambda) + b_{bp}(\lambda). \tag{6b}$$

with subscripts "p, ph, DOM" representing particles, phytoplankton pigments, and dissolved organic matter, respectively. The values of a_w and b_{bw} were adopted from Smith and Baker [22].

The absorption coefficient of phytoplankton pigments ($a_{ph}(\lambda)$) is expressed as

$$a_{ph}(\lambda) = [\text{Chl}] \times a^*_{ph}(\lambda), \tag{7}$$

with $a^*_{ph}(\lambda)$ (the chlorophyll-specific absorption coefficient) taken from Vernet et al. [32].

Spectra of b_{bp} and a_{DOM} are modeled as:

$$a_{DOM}(\lambda) = a_{DOM}(440)\, e^{-S(\lambda-440)}, \tag{8a}$$

$$b_{bp}(\lambda) = b_{bp}(490)(\lambda/490)^{-\eta}, \tag{8b}$$

where the spectral slope (S) of a_{DOM} was taken as 0.017 nm^{-1}, and the backscattering exponent (η) was assumed as 1.0 [33]. Further, following Morel [34], $a_{DOM}(440)$ was assumed as 20% of the sum of ($a_w(440) + a_{ph}(440)$). After $a_{DOM}(440)$ and S values are known, spectrum of $a_{DOM}(\lambda)$ can then be calculated following Eq. 8(a). The value of $b_{bp}(490)$ was estimated based on the standard SeaWiFS product $K_d(490)$ [20,35] through the combination of Eqs. 5–8, which can solve for $b_{bp}(490)$.

Although this complex scheme (V2001) started with the K_d - IOPs model developed by Gordon [28], it relies on [Chl] and $K_d(490)$ as the inputs, where both are empirically estimated from the band ratio of R_{rs}, it is thus essentially a multi-step empirical algorithm for the estimation of $K_d(UV)$.

2.5. Absorption-based empirical method (S2011)

Based on measured data (2007~2009, total 106 data stations), Smyth [15] developed an empirical relationship between $K_d(380)$ and $a(443)$ as:

$$K_d(380) = A(\lambda) \times a(443)^2 + B(\lambda) \times a(443) + C(\lambda) \tag{9}$$

with A, B and C the fitting coefficients for targeted wavelength (380 nm here in particular) [15]. $K_d(305, 325, 340)$ was further empirically linked with $K_d(380)$ [15]. In this system, the required $a(443)$ was derived from a look-up-table algorithm developed by Smyth et al. [36], with data obtained from Hydrolight [37] simulations. Since we don't have the detailed look-up-table of this algorithm, while Smyth [15] showed that this method can obtain similar total absorption as the quasi-analytical algorithm (QAA) [38], here we applied $a(443)$ obtained from QAA to Eq. 9, and focused on $K_d(380)$. We did not evaluate the proposed relationships for $K_d(305, 325, 340)$ [15] as the shortest wavelength from field measurements is 350 nm. Also, note that this system modeled $K_d(305, 325, 340)$ as functions of $K_d(380)$, respectively, which suggests $K_d(UV)$ of different wavelengths co-vary for the global ocean, a relationship not generally supported from measurements [16].

Optics EXPRESS

2.6. Semi-analytical algorithm (L2013)

Through derivations of the radiative transfer equation, Lee et al. [18] found that K_d can be described as a function of a and b_b through

$$K_d(\lambda) = m \times a(\lambda) + v \times b_b(\lambda). \tag{10a}$$

Based on Hydrolight [37] simulations, the two parameters m and v were further described as functions of sun angle and IOPs, and K_d is then expressed as [19]:

$$K_d(\lambda) = (1 + m_0 \times \theta_s)a(\lambda) + (1 - \sigma \times \eta_w(\lambda))m_1(1 - m_2 \times e^{-m_3 \times a(\lambda)})b_b(\lambda), \tag{10b}$$

where θ_s is the solar zenith angle in air (in deg), and $\eta_w = b_{bw}/b_b$. m_{0-3} and σ are model constants and their values are 0.005, 4.259, 0.52, 10.8 and 0.265, respectively [19].

The required inputs for the calculation of K_d are θ_s, a and b_b, with the IOPs ($a\&b_b$) derived following the quasi-analytical algorithm [38]. Its recent version (QAA_v6, https://ioccg.org/wp-content/uploads/2020/11/qaa_v6_202011.pdf) was employed for this study. The contribution of Raman scattering to R_{rs} cannot be ignored for oceanic waters [39], which were removed following the scheme developed in Lee et al. [19].

3. Data

3.1. Field-measured data

Two data sources, which cover waters from the ultra-oligotrophic ocean to turbid coastal waters, are employed in this effort. The measurements of ultra-oligotrophic ocean were around the center of the South Pacific Gyre (SPG, see Fig. 1(*a*)) from the BIOSOPE cruise, which were carried out from 26 October to 11 December 2004 (a total of 25 stations). For these measurements, the concentration of chlorophyll is as low as ~0.01 mg/m^3, while $K_d(380)$ is as low as 0.018 m^{-1} (depth of 1% surface light is deeper than 200 m). There have been many publications about this important and valuable field campaign [40–42], we thus omitted the details here.

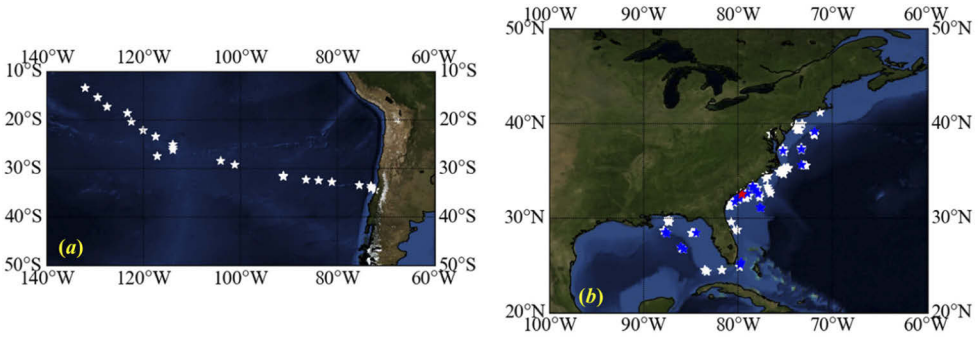

Fig. 1. Locations of field measurements for the evaluation of K_d(UV) algorithms. (*a*) The data came from the BIOSOPE cruise from 26 October to 11 December 2004. (*b*) The data came from the NOAA VIIRS Cal/Val cruise off the East Coast of the United States and the Gulf of Mexico from 2014 to 2019. The white stars are the measurement locations, the blue stars represent stations for satellite and field measurements matched up, with the red star for abnormal data.

Since we are not simply focusing on oceanic waters, measurements of many coastal waters are also included in this effort. Specifically, data from the VIIRS Cal/Val campaigns were utilized, which generally cover waters in the East Coast of the United States [43–47]. The measurements

Optics EXPRESS

were taken from 2014 to 2019 (a total of 294 stations), covered both open ocean and relatively turbid coastal waters (see Fig. 1(*b*)), where $K_d(380)$ is in a range of ~0.026 - 2.34 m^{-1}.

For these VIIRS Cal/Val field measurements, profiles of $L_u(\lambda,z)$ (spectral upwelling radiance, μW cm^{-2} nm^{-1} sr^{-1}) and $E_d(\lambda,z)$ (spectral downwelling irradiance, μW cm^{-2} nm^{-1}) were measured with HyperOCR radiometers manufactured by Satlantic, Inc. The instruments were always deployed in the sunny side of the operation ship and at least 20 m away, with the maximum depth for some of these profiling measurements ~50 m. To minimize uncertainties associated with an individual profiling measurement, following recommendations of the in-water optical measurement protocol [48,49], usually 4 to 5 profiles were taken for each station, which resulted in 100's of measurements per meter, thus allowing an accurate representation of the $L_u(\lambda,z)$ and $E_d(\lambda,z)$ profiles. Further, spectral surface irradiance ($E_s(\lambda)$, μW cm^{-2} nm^{-1}) was simultaneously measured on the ship deck with another HyperOCR radiometer for irradiance. This data was used in the Satlantic Prosoft Version 8.1.6 to remove short-term variations in the incident radiation at sea surface. Note that the spectral range of these HyperOCR is ~350–800 nm, with a spectral bandwidth of 10 nm sampled every 3.3 nm.

From the $E_d(\lambda,z)$ profiles, after excluding data with sensor tilt lager than 5 deg, following Zibordi et al. [50], K_d of each band was calculated as the slope of the linear regression between z and $\ln[E_d(\lambda, z)]$. The depth range for regression is dependent on the wavelength and was set using the optical depth (OD). The shallowest depth used in the regression is 0.5 m from surface, which is the minimum depth a HyperPro can take measurements. The maximum depth used in the regression varies by wavelength and is defined by the maximum optical depth used in the data processing or 20 m whichever is shallower. This maximum optical depth, which varied from 0.5 to 2 for the coastal waters in this study, is determined based on that all the regressions are linear for all wavelengths.

$R_{rs}(\lambda)$ is defined as

$$R_{rs}(\lambda) = \frac{L_w(\lambda)}{E_s(\lambda)}, \tag{11a}$$

where $L_w(\lambda)$ is the spectral water-leaving radiance (μW cm^{-2} nm^{-1} sr^{-1}). For profiling measurements, $L_w(\lambda)$ was derived from the relationship:

$$L_w(\lambda) = \frac{t}{n^2} L_u(0^-, \lambda), \tag{11b}$$

where t is the Fresnel transmittance of radiance from water to air, approximating 0.975. n is the refractive index of water, with a common value as 1.34. $L_u(0^-, \lambda)$ is the upward radiance just beneath the sea surface, which was calculated by extrapolating the $L_u(z, \lambda)$ profile [48] using the Satlantic Prosoft Version 8.1.6. We did not correct the self-shading effect in the $L_u(z, \lambda)$ measurements, as the uncertainty from this factor is just a few percent [49], which is much less than the uncertainties introduced by an algorithm for the inversion of K_d.

For the 294 total stations of clear and cloudy days having HyperPro measurements, it resulted in 291 valid K_d and R_{rs} spectra. The other 3 stations showing abnormal K_d values (approaching 0 at ~500 nm) were excluded in this report, although an inclusion of these stations has negligible impact on the statistics. Fig. 2 shows examples of $R_{rs}(\lambda)$ and $K_d(\lambda)$ spectra from these measurements. As an indicator of the wide coverage of waters included in this effort, the range of $R_{rs}(440)/R_{rs}(550)$ is 0.33 to 13.23.

3.2. Satellite data

To gain insights on applications to satellite ocean color remote sensing, taking the Visible Infrared Imaging Radiometer Suite (VIIRS) as an example, we used satellite-field matchup data to evaluate algorithm estimated K_d(UV). VIIRS Level-2 normalized water-leaving radiance (*nLw*; mW cm^{-2}

Optics EXPRESS

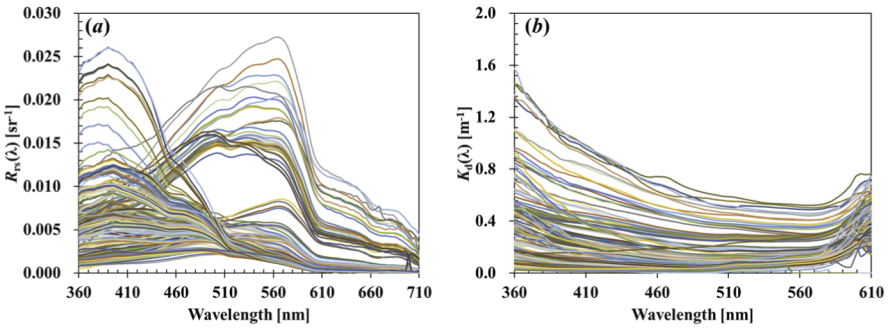

Fig. 2. Examples of field measurements used in this study. (*a*) measured R_{rs} spectra; (*b*) measured K_d spectra.

sr^{-1} μm^{-1}) in the visible band were downloaded from the official website of NOAA CoastWatch (https://coastwatch.noaa.gov). These $nL_w(\lambda)$ were converted to R_{rs} through

$$R_{rs}(\lambda) = \frac{nL_w(\lambda)}{F_0}. \tag{12}$$

where F_0 is the extra-terrestrial solar radiation, which is constant and available in the literature [51].

For a field station, the median value of 3×3 VIIRS pixels centered on this station was used to represent satellite measurement [52]. Further, the time window between *in situ* and satellite data was set as ± 5 hours [53]. Also, the quality of the spectral data was judged according to a quality-assurance (QA) score [54] and Level-2 Processing Flags (l2_flags), where only data with QA score > 0.6 were kept, and excluded VIIRS data containing these l2_flags (atmospheric correction failure, land pixel, probable cloud or ice contamination, strong sun glint contamination and cloud straylight or shadow contamination). We subsequently obtained 62 matchups between VIIRS and field measurements.

3.3. R_{rs}(UV)

Since the shortest band of VIIRS (and SeaWiFS, MODIS, etc.) is ~410 nm, in this study R_{rs} at 360, 380, and 400 nm were generated following a deep-learning scheme ($UVISR_{dl}$) recently developed by Wang et al. [16]. $UVISR_{dl}$ has 4 hidden layers along with various neurons; it uses R_{rs}(visible) as the input to generate R_{rs}(UV), with the estimated R_{rs}(UV) found matching field-measured value within ~10%. The details of $UVISR_{dl}$ can be found in Wang et al. [16].

To be consistent with satellite applications, for the evaluation of L2013 using field measurements that requires R_{rs}(UV) for the analytical calculation of K_d(UV), the field dataset also employed $UVISR_{dl}$ to obtain R_{rs}(UV), although there are R_{rs}(UV) data available from the profiling measurements. In short, for the evaluation of the six algorithms, it is the same visible R_{rs} spectrum applied to all algorithms.

3.4. Accuracy assessment

To quantify the accuracy of the estimated K_d(UV), the following statistical indicators are used for quantitative evaluation: root mean square difference (RMSD), mean absolute relative difference (MARD), mean absolute unbiased relative difference (MAURD), bias and coefficient

Optics EXPRESS

of determination (R^2). They are defined as follows (N is the number of samples):

$$\mathrm{RMSD} = \sqrt{\frac{\sum_{i=1}^{N} (X_{\mathrm{est,i}} - X_{\mathrm{mea,i}})^2}{N}}, \tag{13}$$

$$\mathrm{MARD} = \frac{1}{N} \sum_{i=1}^{N} \frac{|X_{\mathrm{est,i}} - X_{\mathrm{mea,i}}|}{X_{\mathrm{mea,i}}}, \tag{14}$$

$$\mathrm{MAURD} = \frac{1}{N} \sum_{i=1}^{N} \left| \frac{X_{\mathrm{est,i}} - X_{\mathrm{mea,i}}}{X_{\mathrm{est,i}} + X_{\mathrm{mea,i}}} \right| \times 2, \tag{15}$$

$$\mathrm{bias} = \frac{1}{N} \sum_{i=1}^{N} (X_{\mathrm{est,i}} - X_{\mathrm{mea,i}}) \tag{16}$$

where $X_{\mathrm{est,i}}$ and $X_{\mathrm{mea,i}}$ are algorithm estimate and field measurement of K_d(UV), respectively.

4. Results and discussion

4.1. Evaluation of K_d(UV) from field-measured reflectance

The above-described six empirical and semi-analytical algorithms for the estimation of K_d(UV) were evaluated with the dataset described in Section 3, which covers waters from the oligotrophic ocean to coastal areas. Figs. 3~4 and Table 1 summarize the performance of these algorithms, where some of these algorithms [9,11,14,15] focused on K_{d}(380) and/or other specific wavelengths (Fig. 3), while the other three algorithms also cover 360 nm and 400 nm (Fig. 4). Outcomes of each algorithm are described below.

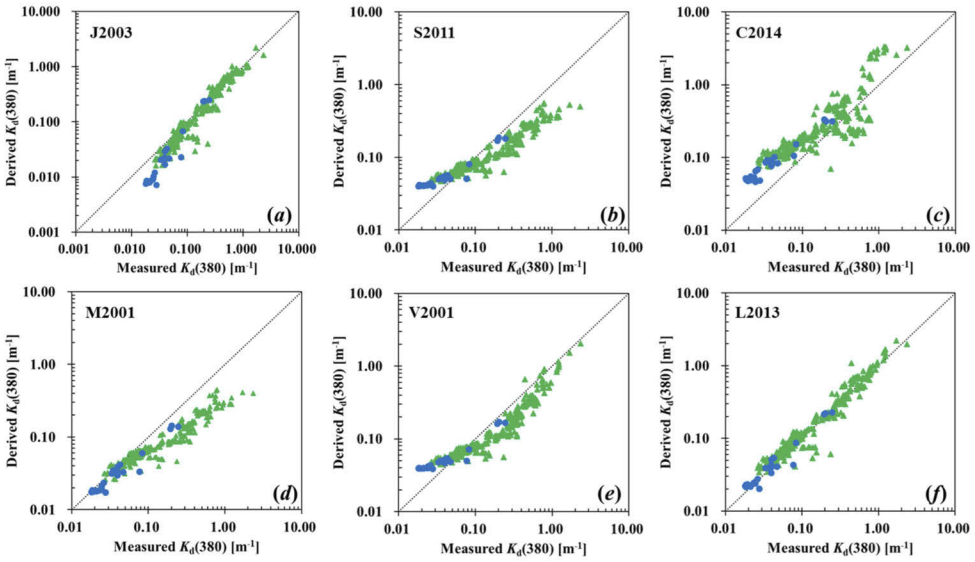

Fig. 3. Comparison between measured and algorithm-estimated K_{d}(380) (the blue dots represent data from the BIOSOPE cruise, the green dots represent data from the NOAA Cal/Val cruise). (*a*) J2003, (*b*) S2011, (*c*) C2014, (*d*) M2001, (*e*) V2001, (*f*) L2013.

4.1.1. J2003

The empirical algorithm (J2003) for K_d(380) developed by Johannessen et al. (2003) is one of the earlier attempts for the estimation of K_d(UV) from ocean color measurements. For this

Optics EXPRESS

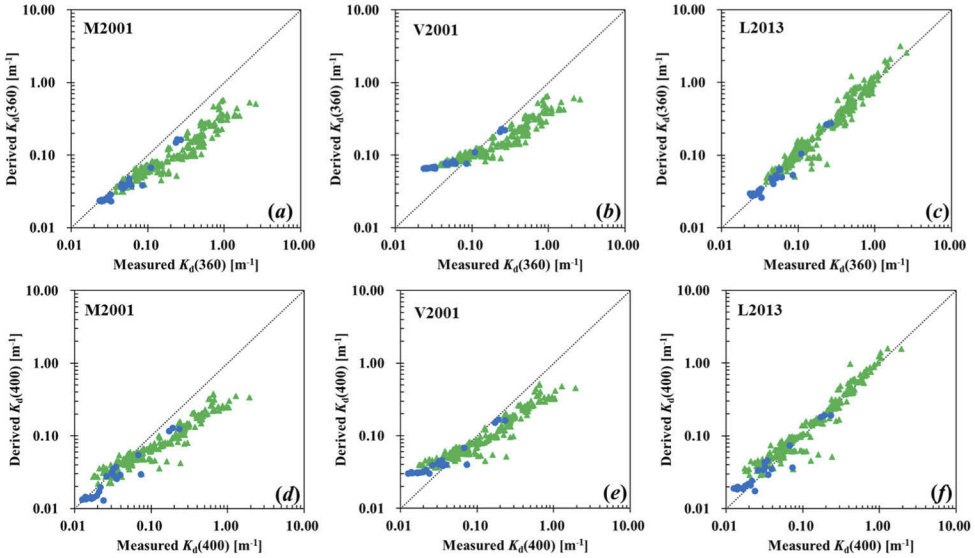

Fig. 4. As Fig. 3, but for $K_d(360)$ ((*a*) M2001, (*b*) V2001, (*c*) L2013) and $K_d(400)$ ((*d*) M2001, (*e*) V2001, (*f*) L2013).

Table 1. $K_d(360)$, $K_d(380)$ and $K_d(400)$ algorithm inversion results statistical analysis.

Model	Band	Data Number	RMSD (m^{-1})	MARD	MAURD	bias (m^{-1})	R^2
M(2001)	$K_d(360)$	316	0.30	0.44	0.61	-0.17	0.81
V(2001)			0.26	0.41	0.45	-0.13	0.82
L(2013)			0.12	0.17	0.16	0.029	0.93
M(2001)	$K_d(380)$	316	0.24	0.38	0.52	-0.13	0.81
V(2001)			0.21	0.36	0.41	-0.10	0.82
J(2003)			0.082	0.23	0.27	-0.0017	0.92
S(2011)			0.12	0.31	0.35	-0.067	0.91
L(2013)			0.083	0.19	0.18	0.019	0.94
C(2014)			0.40	0.90	0.59	0.13	0.70
M(2001)	$K_d(400)$	316	0.20	0.35	0.45	-0.099	0.83
V(2001)			0.17	0.34	0.37	-0.073	0.84
L(2013)			0.065	0.22	0.20	0.016	0.94

evaluation dataset where $K_d(380)$ is in a range of 0.018–2.34 m^{-1}, J2003 performed very well (Fig. 3(*a*)). The values of RMSD, MARD, and R^2 are just slightly worse than that of L2013 (Table 1). This is likely due to that this empirical algorithm was developed also based on data measured in the East Coast of the United States ($K_d(380)$ was in a range of 0.033–4.39 m^{-1}), where there are similar data characteristics between the data for algorithm development and data for algorithm evaluation. For the lower end of $K_d(380)$ (<0.1 m^{-1}) mostly obtained from the BIOSOPE cruise, types of waters not covered by Johannessen et al. [11] in the phase of algorithm development, $K_d(380)$ estimated by J2003 appeared generally underestimated (by ~47%) compared to field-measured $K_d(380)$. This degraded performance is expected when the application of an empirical algorithm is extended beyond its range. Note that, if the true $K_d(380)$ is 0.02 m^{-1}, a 47% underestimation will result in ~1.5 times more estimation of UV radiation at 100 m, thus significantly over-emphasize the impact of UV.

Optics EXPRESS

4.1.2. S2011

S2011 is an empirical algorithm centered on the total absorption coefficient for $K_d(380)$, which performed reasonably well for this evaluation dataset (see Fig. 3(*b*)). However, the performance is not uniform across the values of $K_d(380)$, where S2011 underestimated (by 39%) $K_d(380)$ for values ~0.1 - 1.0 m^{-1}. On the other hand, for $K_d(380)$ lower than about 0.04 m^{-1}, S2011 overestimated $K_d(380)$ by about 58%, which is likely due to that the range of $K_d(380)$ is higher than the lower limit of ~0.04 m^{-1} when S2011 was developed. This overestimation of $K_d(380)$ will significantly under-represent UV radiation at deeper depths (by a factor about 3 at 100 m). In addition to the data dependency of any empirical algorithms, another reason for the deviations of S2011 is likely in the model itself (Eq. 9), where $K_d(380)$ is simply modeled as a second-order polynomial function of $a(443)$. However, radiative transfer indicates that K_d is jointly determined by both a and b_b, thus uneven performance will be resulted when there are different levels of contributions from backscattering.

4.1.3. C2014

C2014 uses PCA to reduce the dimension of R_{rs}, and then relates $K_d(380)$ with the scores of the pre-established principal components through a multiple-component regression. This algorithm does not perform well for this evaluation dataset (see Fig. 3(*c*), Table 1). For $K_d(380) <$ ~0.05 m^{-1}, C2014 overestimated $K_d(380)$ by more than 100%, which, similarly as the results of S2011, is likely due to that the lower limit of $K_d(380)$ is ~0.05 m^{-1} when SeaUVc was developed (Fichot et al. [9]). The meaning of the principal components derived from a group of R_{rs} spectra is vague, thus the physics of a PCA-based algorithm for an optical or geophysical property is not straightforward. Further, since the principal components are data dependent, the performance of such kind of algorithms may vary for different datasets.

4.1.4. M2001

The two-steps scheme (M2001) based on Morel and Maritorena [12] performed better at the lower end ($K_d(380) <$ ~0.06 m^{-1}) for the three wavelengths (360, 380, and 400 nm) evaluated here, but generally underestimated (by ~57%) $K_d(UV)$ for $K_d(380) > 0.1$ m^{-1} (see Figs. 3(*d*), 4(*a*), and 4(*d*)). The Morel and Maritorena [12] system was developed based on a large dataset mostly collected in oceanic waters ($K_d(420)$ is in a range of 0.007 - 0.94 m^{-1}), but most of the measurements of this evaluation dataset were from coastal waters, which might explain the very good performance at the lower end (including the ultra-oligotrophic ocean), but unsatisfactory results for coastal waters.

4.1.5. V2001

Similar as M2001, V2001 estimates $K_d(UV)$ based on the "Case 1" concept, but taking a much more complex data processing scheme. For this evaluation dataset that covers both oceanic and coastal waters. Interestingly, similarly as M2001, V2001 also underestimated $K_d(UV)$ for $K_d(380) > 0.1$ m^{-1} (see Figs. 3(e), 4(b), and 4(e)), but this underestimation (~44%) is not as severe as that of M2001. But for the lower end ($K_d(380) <$ ~0.03 m^{-1}), V2001 significantly (89%) overestimated $K_d(UV)$ (see Figs. 3(e), 4(b), and 4(e)), likely due to an extension of this algorithm beyond its limit (the lower end was 0.03 m^{-1} when the algorithm was developed). It is found that the estimated $K_d(400)$ agreed better with field measurements compared to $K_d(360)$ (see Table 1), which in part is due to the selection of the S value in the system (Eq. 8a), as a large S value (0.017 nm^{-1}) suggests higher estimation of $a_{DOM}(360)$ due to the exponential function, which further propagates to the estimated $K_d(360)$. For oceanic waters, Bricaud et al. [55] suggested that S is around 0.014 nm^{-1}.

Optics EXPRESS

4.1.6. L2013

L2013 is an algorithm centered on the IOPs (absorption and backscattering coefficients in particular), with the relationship established from the radiative transfer equation. More importantly, contrary to empirical algorithms, the algorithm coefficients of L2013 were not derived from any datasets obtained from field measurements, thus theoretically its application to an R_{rs} spectrum is not subjective to datasets. As a result, it is not surprising to see that L2013 has the best performance among the six algorithms for this evaluation dataset that covers wide range of waters (see Figs. 3(f), 4(c), 4(f), and Table 1). Especially, the performance is uniform for $K_{\mathrm{d}}(380)$ in a range of ~0.02–2.0 m^{-1}, rather showing any obvious deviations for any specific ranges or values of $K_{\mathrm{d}}(\mathrm{UV})$. This further highlights the power of systems based on radiative transfer, where the performance is the same for all waters and for all wavelengths, instead of varying performances with water types or wavelengths showing by the empirical algorithms (e.g., J2003, S2011). In addition, these results further support the deep-learning system (Wang et al. 2021) for the estimation of $R_{\mathrm{rs}}(\mathrm{UV})$ as well as QAA for the algebraic derivation of IOPs from an R_{rs} spectrum, for waters from ultra-oligotrophic ocean to coastal waters.

4.2. Evaluation of VIIRS K_d(UV) with in situ measurements

Since the ultimate goal of an algorithm is to apply it to ocean color satellites to obtain global distribution of $K_d(\mathrm{UV})$, here we further evaluated $K_d(\mathrm{UV})$ obtained by VIIRS measurements, where the locations of the satellite-insitu matchup stations are shown in Fig. 1(b) with blue stars. As the other five algorithms showed limited accuracy to some waters, the evaluation is focused on $K_{\mathrm{d}}(\mathrm{UV})$ from L2013 only. Also included for this comparison is $K_{\mathrm{d}}(410, 443, 486)$ obtained from L2013. Fig. 5 (*a* - *f*) presents scatterplots between inversion and measured K_d ($K_{\mathrm{d}}(360)$ is in a range of 0.046–0.84 m^{-1}), while statistical measures are presented in Table 2.

Table 2. Statistical analysis between matchup VIIRS and *in situ* $K_{\mathrm{d}}(\lambda)$. N for the number of matchup stations.

Band	Data Number (N)	RMSD (m^{-1})	MARD	MAURD	bias (m^{-1})	R^2
360	62	0.090	0.19	0.21	-0.031	0.92
380		0.071	0.21	0.22	-0.022	0.94
400		0.065	0.26	0.25	-0.020	0.95
410		0.065	0.27	0.25	-0.021	0.95
443		0.052	0.28	0.25	-0.015	0.96
486		0.047	0.27	0.25	-0.015	0.96

Overall, for these $K_d(\mathrm{UV})$, the R^2 values are greater than 0.92, with MARD between 0.19 (at 360 nm) and 0.28 (at 443 nm), and bias in a range of ~ -0.031 to -0.015 m^{-1}. These evaluation indicators are slightly worse than that obtained from the field-measured R_{rs}, a result not surprising for ocean color satellite remote sensing. Reasons contributing to this lowered performance include: 1) No exact "matchup" between satellite and field measurements due to gaps in time and space [56,57], which is one of the major sources of data deviation [53]. 2) Imperfect atmosphere correction in both oceanic and coastal areas [58–61], consequently the errors in the *nLw* (R_{rs}) product will be propagated to those further estimated from R_{rs}. Fig. 5 (*d* - *f*) compares VIIRS $K_d(410, 443, 486)$ with *in situ* $K_d(410, 443, 486)$, where the MARD values range are ~ 0.27 - 0.28 and RMSD ~ 0.050 m^{-1}, which are just slightly better than those of $K_d(\mathrm{UV})$, further indicating the deep-learning estimated $R_{\mathrm{rs}}(\mathrm{UV})$ has similar quality as those of R_{rs} in the visible (Wang et al. 2021).

There are a few stations (the red triangles in Fig. 5) where VIIRS $K_d(360 - 486)$ are much lower than *in situ* K_d ($K_d(360)$ is around 1.0 m^{-1}). These four stations were from a nearshore

Optics EXPRESS

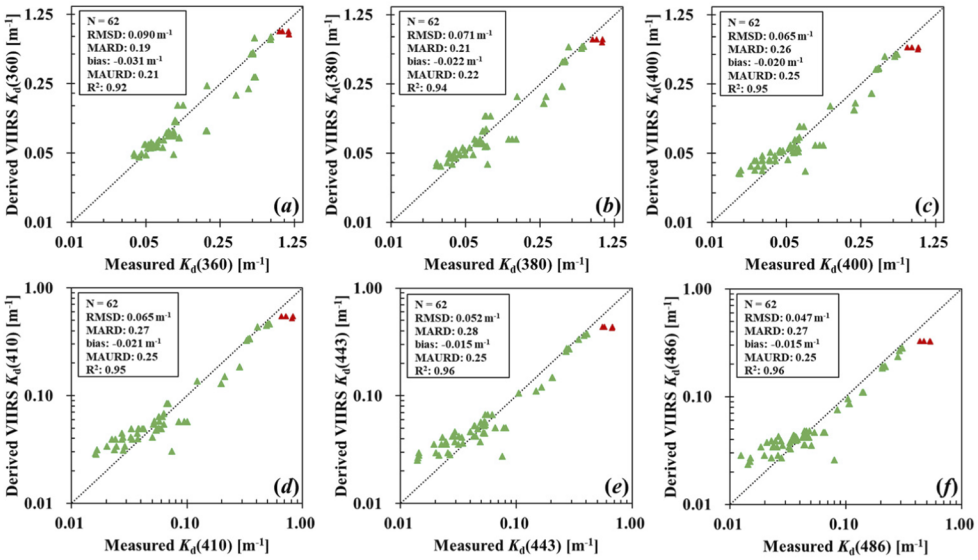

Fig. 5. Comparison between VIIRS and measured K_d. (*a*) $K_d(360)$, (*b*) $K_d(380)$, (*c*) $K_d(400)$, (*d*) $K_d(410)$, (*e*) $K_d(443)$, and (*f*) $K_d(486)$. The red triangles represent the matching data of the red-star location in Fig. 1(b).

area (Fig. 1(b), the red star) and collected on Oct. 14, 2016. Based on the VIIRS Level-2 flags processed by NOAA MSL12, there are stray-light contaminations in this VIIRS image, which may be the reason for the larger deviation of these stations. In addition, there was heavy stratification in these coastal waters with a high-sediment fresh-water layer at the surface from runoff due to Hurricane Matthew. This complicates satellite measures to the corresponding profiles [62].

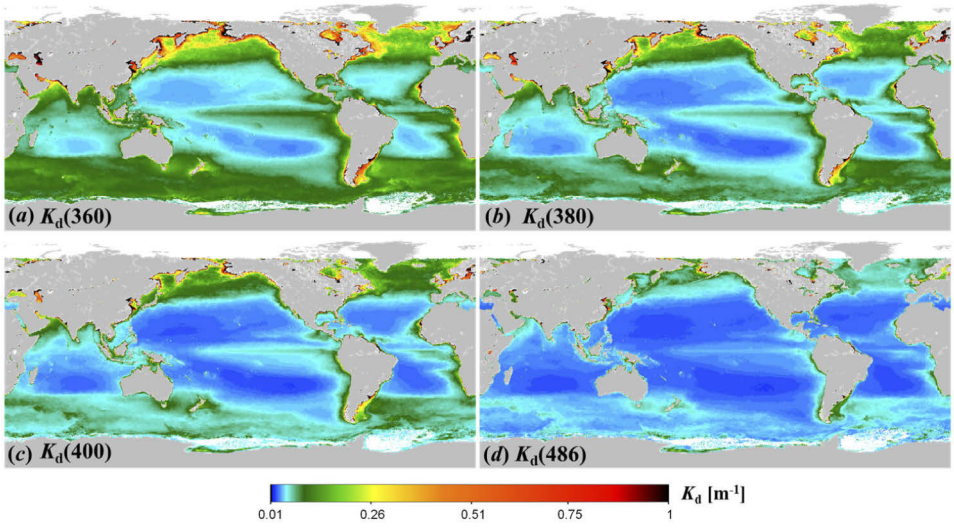

Fig. 6. Global distribution of VIIRS $K_d(\lambda)$ climatology data. (*a*) $K_d(360)$, (*b*) $K_d(380)$, (*c*) $K_d(400)$, (*d*) $K_d(486)$.

Optics EXPRESS

4.3. K_d(UV) of global ocean from VIIRS

As the above shows very good estimation of K_d(UV) from VIIRS, examples of K_d(360, 380, 400 and 486 (with the Sun at zenith) of the global ocean are produced from VIIRS for climatology R_{rs} (see Fig. 6). Compared to the partial K_d(360) map obtained by Lee et al. [19], the results extend the estimation of K_d(UV) to the global ocean, which then help providing solar radiation distribution in the upper column for the evaluation of photochemical and photobiological processes in the ocean.

Spatially, while K_d(380) is as low as ~0.02 m^{-1} at the South Pacific Gyre, but due to the influence of terrestrial sources [15], K_d(380) can be as high as ~3.0 m^{-1} in coastal regions such as the Yangtze Estuary. If the depth of 10% surface light can be a measure of the penetration of solar radiation, the penetration depth of solar radiation at 380 nm is ~100 m at South Pacific Gyre. Such a strong penetration is expected to have comprehensive impacts on biogeochemical processes in the oceans [63,64].

5. Conclusions

From a large dataset covering super clear ocean gyre waters and coastal turbid waters, six empirical and semi-analytical algorithms developed for the estimation of K_d(UV) from the measurement of ocean color were evaluated. The five empirical algorithms showed reasonable results for some K_d(UV) values or waters, but indicated limitations for other waters, suggesting challenges to apply such empirical algorithms for the generation of K_d(UV) for the global oceans from satellite ocean color missions. The semi-analytical algorithm centered on waters' inherent optical properties, however, not only obtained the best estimates compared to field measurements, also show uniform performance from ultra-oligotrophic ocean to coastal waters, as well as for the three wavelengths in the UV evaluated. These results further highlight the power of algorithms based on the radiative transfer, which is not limited to a single wavelength (such as the empirical algorithms for K_d(490) or K_d(380), for instance), rather applicable for an accurate estimation of a K_d spectrum, as long as the spectra of the total absorption and backscattering can be accurately produced from an R_{rs} spectrum. Also, the excellent agreement between K_d estimated from VIIRS ocean color data (with the semi-analytical algorithm) and field measurements indicates that VIIRS normalized water-leaving radiance (equivalent to R_{rs}) has very high quality. On the other hand, it is necessary to keep in mind that this dataset does not include waters with phytoplankton blooms containing mycosporine-like amino acids (MAAs). Due to the strong absorption of MAAs in the UV domain [65,66], the remote sensing of K_d(UV) for such kind of waters deserve further studies.

To summarize, with the deep learning system developed for the estimation of R_{rs}(UV) in the near-blue domain from R_{rs} in the visible, it is now feasible to produce highly reliable K_d(UV) from ocean color satellites dating back to the SeaWiFS, MODIS era. A generation of global data product in the past 20 + years will then lay the foundation for the study of long-term interactions between UV radiation and biogeochemical processes in the global ocean.

Funding. Ministry of Science and Technology of the People's Republic of China (2018YFC1407506); National Natural Science Foundation of China (#41830102, #41890803, #41941008); NOAA ocean color calibration and validation; University of Massachusetts Boston.

Acknowledgments. We are grateful to Dr. Marlon Lewis for sharing profiling measurements obtained during the BIOSOPE cruise and NOAA STAR for providing VIIRS Ocean Color measurements. Comments and suggestions from four anonymous reviewers are greatly appreciated. The views, opinions, and findings contained in this paper are those of the authors and should not be construed as an official NOAA or U.S. Government position, policy, or decision.

Disclosures. The authors declare no conflicts of interest.

Data availability. Data used in this study are available in either NASA SeaBASS or NOAA data portal, can also be obtained from the authors upon request.

Optics EXPRESS

References

1. M. Tedetti and R. Sempéré, "Penetration of ultraviolet radiation in the marine environment. A review," Photochem Photobiol **82**(2), 389–397 (2006).
2. K. Gao, E. W. Helbling, D.-P. Häder, and D. A. Hutchins, "Responses of marine primary producers to interactions between ocean acidification, solar radiation, and warming," Mar. Ecol. Prog. Ser. **470**, 167–189 (2012).
3. R. Zepp, D. Erickson Iii, N. Paul, and B. Sulzberger, "Interactive effects of solar UV radiation and climate change on biogeochemical cycling," Photochem. Photobiol. Sci. **6**(3), 286–300 (2007).
4. C. Piccini, D. Conde, J. Pernthaler, and R. Sommaruga, "Alteration of chromophoric dissolved organic matter by solar UV radiation causes rapid changes in bacterial community composition," Photochem. Photobiol. Sci. **8**(9), 1321–1328 (2009).
5. K. C. Rose, C. E. Williamson, J. M. Fischer, S. J. Connelly, M. Olson, A. J. Tucker, and D. A. Noe, "The role of ultraviolet radiation and fish in regulating the vertical distribution of Daphnia," Photochem. Photobiol. Sci. **57**(6), 1867–1876 (2012).
6. A. McLeod, T. Brand, C. Campbell, K. Davidson, and A. Hatton, "Ultraviolet radiation drives emission of climate-relevant gases from marine phytoplankton," Journal of Geophysical Research: Biogeosciences, e2021JG006345 (2021).
7. C. Booth and J. Morrow, "The penetration of UV into natural waters," Photochem Photobiol **65**, 254–257 (1997).
8. R. W. Preisendorfer, "Secchi disk science: Visual optics of natural waters," Photochem. Photobiol. Sci. **31**(5), 909–926 (1986).
9. C. G. Fichot, S. Sathyendranath, and W. L. Miller, "SeaUV and SeaUVC: Algorithms for the retrieval of UV/Visible diffuse attenuation coefficients from ocean color," Remote Sensing of Environment **112**, 1584–1602 (2008).
10. A. Vasilkov, N. Krotkov, J. Herman, C. McClain, K. Arrigo, and W. Robinson, "Global mapping of underwater UV irradiances and DNA-weighted exposures using Total Ozone Mapping Spectrometer and Sea-viewing Wide Field-of-view Sensor data products," J. Geophys. Res. **106**(C11), 27205–27219 (2001).
11. S. C. Johannessen, W. L. Miller, and J. J. Cullen, "Calculation of UV attenuation and colored dissolved organic matter absorption spectra from measurements of ocean color," J. Geophys. Res. **108**(C9), 3301 (2003).
12. A. Morel and S. Maritorena, "Bio-optical properties of oceanic waters: A reappraisal," J. Geophys. Res. **106**(C4), 7163–7180 (2001).
13. K. Sun, T. Zhang, S. Chen, C. Xue, B. Zou, and L. Shi, "Retrieval of Ultraviolet Diffuse Attenuation Coefficients From Ocean Color Using the Kernel Principal Components Analysis Over Ocean," IEEE Transactions on Geoscience and Remote Sensing **59**(6), 4579–4589 (2021).
14. F. Cao, C. G. Fichot, S. B. Hooker, and W. L. Miller, "Improved algorithms for accurate retrieval of UV/visible diffuse attenuation coefficients in optically complex, inshore waters," Remote sensing of environment **144**, 11–27 (2014).
15. T. J. Smyth, "Penetration of UV irradiance into the global ocean," J. Geophys. Res. **116**(C11), 2011JC007183 (2011).
16. Y. Wang, Z. Lee, J. Wei, S. Shang, M. Wang, and W. Lai, "Extending satellite ocean color remote sensing to the near-blue ultraviolet bands," Remote Sensing of Environment **253**, 112228 (2021).
17. H. Liu, X. He, Q. Li, S. Kratzer, J. Wang, T. Shi, Z. Hu, C. Yang, S. Hu, and Q. Zhou, "Estimating ultraviolet reflectance from visible bands in ocean colour remote sensing," Remote Sensing of Environment **258**, 112404 (2021).
18. Z. P. Lee, K. P. Du, and R. Arnone, "A model for the diffuse attenuation coefficient of downwelling irradiance," J. Geophys. Res. **110**(C2), C02016 (2005).
19. Z. Lee, C. Hu, S. Shang, K. Du, M. Lewis, R. Arnone, and R. Brewin, "Penetration of UV-visible solar radiation in the global oceans: Insights from ocean color remote sensing," J. Geophys. Res. **118**(9), 4241–4255 (2013).
20. J. L. Mueller, "SeaWiFS algorithm for the diffuse attenuation coefficient, K(490), using water-leaving radiances at 490 and 555 nm," in *SeaWiFS Postlaunch Calibration and Validation Analyses, Part 3*, S. B. Hooker, ed. (NASA, 2000), 24–27.
21. R. W. Austin and T. J. Petzold, "The determination of the diffuse attenuation coefficient of sea water using the coastal zone color scanner," in *Oceanography from Space*, J. F. R. Gower, ed. (Plenum Press, 1981), pp. 239-256.
22. R. C. Smith and K. S. Baker, "Optical properties of the clearest natural waters," Appl. Opt. **20**(2), 177–184 (1981).
23. R. Pope and E. Fry, "Absorption spectrum (380 - 700 nm) of pure waters: II. Integrating cavity measurements," Appl. Opt. **36**(33), 8710–8723 (1997).
24. A. Morel, "Optical properties of pure water and pure sea water," in *Optical Aspects of Oceanography*, N. G. Jerlov and E. S. Nielsen, eds. (Academic, 1974), pp. 1-24.
25. Z. Lee, J. Wei, K. Voss, M. Lewis, A. Bricaud, and Y. Huot, "Hyperspectral absorption coefficient of "pure" seawater in the range of 350–550 nm inverted from remote sensing reflectance," Appl. Opt. **54**(3), 546–558 (2015).
26. X. Zhang and L. Hu, "Estimating scattering of pure water from density fluctuation of the refractive index," Opt. Express **17**(3), 1671–1678 (2009).
27. J. E. O'Reilly, S. Maritorena, B. G. Mitchell, D. A. Siegel, K. L. Carder, S. A. Garver, M. Kahru, and C. McClain, "Ocean color chlorophyll algorithms for SeaWiFS," J. Geophys. Res. **103**(C11), 24937–24953 (1998).
28. H. R. Gordon, "Dependence of the diffuse reflectance of natural waters on the sun angle," Photochem. Photobiol. Sci. **34**(8), 1484–1489 (1989).
29. K. L. Carder, S. K. Hawes, K. A. Baker, R. C. Smith, R. G. Steward, and B. G. Mitchell, "Reflectance model for quantifying chlorophyll a in the presence of productivity degradation products," J. Geophys. Res. **96**(C11), 20599–20611 (1991).

Optics EXPRESS

30. L. Prieur and S. Sathyendranath, "An optical classification of coastal and oceanic waters based on the specific spectral absorption curves of phytoplankton pigments, dissolved organic matter, and other particulate materials 1," Photochem. Photobiol. Sci. **26**(4), 671–689 (1981).
31. R. P. Bukata, J. H. Jerome, K. Y. Kondratyev, and D. V. Pozdnyakov, *Optical Properties and Remote Sensing of Inland and Coastal Waters* (CRC Press, 1995).
32. M. Vernet, E. A. Brody, O. Holm-Hansen, and B. G. Mitchell, "The response of Antarctic phytoplankton to ultraviolet radiation: absorption, photosynthesis, and taxonomic composition," Ultraviolet radiation in Antarctica: measurements and biological effects **62**, 143–158 (1994).
33. H. R. Gordon and A. Morel, *Remote assessment of ocean color for interpretation of satellite visible imagery: A review* (Springer-Verlag, 1983).
34. A. Morel, "Optical modeling of the upper ocean in relation to its biogenous matter content (case I waters)," J. Geophys. Res. **93**(C9), 10749–10768 (1988).
35. C. R. McClain, W. E. Esaias, W. Barnes, B. Guenther, D. Endres, S. B. Hooker, G. Mitchell, and R. Barnes, "Calibration and validation plan for SeaWiFS., " in NASA Tech. Memo., 104566, Vol. 3 S. B. Hooker and E. R. Firestone, eds. (NASA Goddard Space Flight Center, 1992), p. 41.
36. T. J. Smyth, G. F. Moore, T. Hirata, and J. Aiken, "Semianalytical model for the derivation of ocean color inherent optical properties: description, implementation, and performance assessment," Appl. Opt. **45**(31), 8116–8131 (2006).
37. C. D. Mobley, "Hydrolight 3.0 Users' Guide," (SRI International, 1995).
38. Z. P. Lee, K. L. Carder, and R. Arnone, "Deriving inherent optical properties from water color: A multi-band quasi-analytical algorithm for optically deep waters," Appl. Opt. **41**(27), 5755–5772 (2002).
39. T. K. Westberry, E. Boss, and Z. Lee, "The Influence of Raman Scattering on Ocean Color Inversion Models," Appl. Opt., under revision (2013).
40. M. Tedetti, R. Sempéré, A. Vasilkov, B. Charrière, D. Nérini, W. L. Miller, K. Kawamura, and P. Raimbault, "High penetration of ultraviolet radiation in the south east Pacific waters," Geophysical Research Letters, 34 (2007).
41. A. Morel, B. Gentili, H. Claustre, A. Babin, A. Bricaud, J. Ras, and F. Tieche, "Optical properties of the "clearest" natural waters," Limnol. Oceanogr. **52**(1), 217–229 (2007).
42. M. Twardowski, H. Claustre, S. Freeman, D. Stramski, and Y. Huot, ""Optical backscattering properties of the" clearest" natural waters," Biogeosciences **4**(6), 1041–1058 (2007).
43. M. Ondrusek, V. P. Lance, M. Wang, E. Stengel, C. Kovach, S. Freeman, A. Mannino, A. Gilerson, C. Carrizo, and P. Grötsch, "Report for Dedicated JPSS VIIRS Ocean Color Calibration/Validation Cruise September 2019," (2021).
44. M. Ondrusek, V. P. Lance, M. Wang, E. Stengel, C. Kovach, R. A. Arnone, S. Ladner, W. Goode, A. Gilerson, and A. El-Habashi, "Report for Dedicated JPSS VIIRS Ocean Color Calibration/Validation Cruise May 2018," (2019).
45. M. Ondrusek, V. P. Lance, M. Wang, E. Stengel, C. Kovach, R. A. Arnone, S. Ladner, W. Goode, A. Gilerson, and S. A. Ahmed, "Report for dedicated JPSS VIIRS Ocean Color Calibration/Validation Cruise, October 2016," (2017).
46. M. Ondrusek, V. P. Lance, M. Wang, R. A. Arnone, S. Ladner, W. Goode, R. Vandermeulen, S. Freeman, J. E. Chaves, and A. Mannino, "Report for dedicated JPSS VIIRS ocean color December 2015 calibration/validation cruise," (2016).
47. M. Ondrusek and V. P. Lance, "Report for dedicated JPSS VIIRS ocean color calibration/validation cruise," (2015).
48. J. L. Mueller, A. Morel, R. Frouin, C. Davis, R. Arnone, K. Carder, Z. Lee, R. Steward, S. Hooker, and C. Mobley, "Ocean Optics Protocols For Satellite Ocean Color Sensor Validation, Revision 4. Volume III: Radiometric Measurements and Data Analysis Protocols," (2003).
49. G. Zibordi, K. J. Voss, B. C. Johnson, and J. Mueller, "IOCCG Ocean optics and biogeochemistry protocols for satellite ocean colour sensor validation," IOCCG Protocols Series 3 (2019).
50. G. Zibordi, K. Ruddick, I. Ansko, G. Moore, S. Kratzer, J. Icely, and A. Reinart, "In situ determination of the remote sensing reflectance: an inter-comparison," Ocean Science **8**(4), 567–586 (2012).
51. G. Thuillier, M. Hersé, T. Foujols, W. Peetermans, D. Gillotay, P. Simon, and H. Mandel, "The solar spectral irradiance from 200 to 2400 nm as measured by the SOLSPEC spectrometer from the ATLAS and EURECA missions," Solar Physics **214**(1), 1–22 (2003).
52. S. W. Bailey and P. J. Werdell, "A multi-sensor approach for the on-orbit validation of ocean color satellite data products," Remote Sens. Environ. **102**(1-2), 12–23 (2006).
53. P. J. Werdell and S. W. Bailey, "An improved in-situ bio-optical data set for ocean color algorithm development and satellite data product validation," Remote sensing of environment **98**(1), 122–140 (2005).
54. J. Wei, Z. Lee, and S. Shang, "A system to measure the data quality of spectral remote-sensing reflectance of aquatic environments," J. Geophys. Res. 121, 8189–8207 (2016).
55. A. Bricaud, A. Morel, and L. Prieur, "Absorption by Dissolved Organic Matter of the Sea (Yellow Substance) in the UV and Visible Domains," Photochem. Photobiol. Sci. **26**(1), 43–53 (1981).
56. D. Antoine, F. d'Ortenzio, S. B. Hooker, G. Bécu, B. Gentili, D. Tailliez, and A. J. Scott, "Assessment of uncertainty in the ocean reflectance determined by three satellite ocean color sensors (MERIS, SeaWiFS and MODIS-A) at an offshore site in the Mediterranean Sea (BOUSSOLE project)," J. Geophys. Res. **113**(C7), C07013 (2008).
57. G. Zibordi, J.-F. Berthon, F. Mélin, D. D'Alimonte, and S. Kaitala, "Validation of satellite ocean color primary products at optically complex coastal sites: Northern Adriatic Sea, Northern Baltic Proper and Gulf of Finland," Remote Sensing of Environment **113**(12), 2574–2591 (2009).

Optics EXPRESS

58. J. Wei, Z. Lee, R. Garcia, L. Zoffoli, R. A. Armstrong, Z. Shang, P. Sheldon, and R. F. Chen, "An assessment of Landsat-8 atmospheric correction schemes and remote sensing reflectance products in coral reefs and coastal turbid waters," Remote sensing of environment **215**, 18–32 (2018).
59. IOCCG, "Atmospheric Correction for Remotely-Sensed Ocean-Colour Products," in *Reports of the International Ocean-Colour Coordinating Group*, M. Wang, ed. (IOCCG, 2010), p. 83.
60. M. Wang, "Remote sensing of the ocean contributions from ultraviolet to near-infrared using the shortwave infrared bands: simulations," Appl. Opt. **46**(9), 1535–1547 (2007).
61. J. Wang, Z. Lee, J. Wei, and K. Du, "Atmospheric correction in coastal region using same-day observations of different sun-sensor geometries with a revised POLYMER model," Opt. Express **28**(18), 26953–26976 (2020).
62. Z. Lee, S. Shang, Y. Wang, J. Wei, and J. Ishizaka, "Nature of optical products inverted semianalytically from remote sensing reflectance of stratified waters," Photochem. Photobiol. Sci. (2019).
63. J. J. Cullen and P. J. Neale, "Ultraviolet radiation, ozone depletion, and marine photosynthesis," Photosynthesis Research **39**(3), 303–320 (1994).
64. R. C. Smith, B. Prezelin, K. e. a. Baker, R. Bidigare, N. Boucher, T. Coley, D. Karentz, S. MacIntyre, H. Matlick, and D. Menzies, "Ozone depletion: ultraviolet radiation and phytoplankton biology in Antarctic waters," Science **255**(5047), 952–959 (1992).
65. M. Kahru, C. Anderson, A. D. Barton, M. L. Carter, D. Catlett, U. Send, H. M. Sosik, E. L. Weiss, and B. G. Mitchell, "Satellite detection of dinoflagellate blooms off California by UV reflectance ratios," Elem Sci Anth **9**(1), 00157 (2021).
66. M. Kahru and B. G. Mitchell, "Spectral reflectance and absorption of a massive red tide off southern California," J. Geophys. Res. **103**(C10), 21601–21609 (1998).